Process parameter development and optimization for the Scalmalloy® alloy in the additive manufacturing of aircraft applications

Jens Niedermeyer[a], Timo Witte[a], Fabian Schlenker[c], Jan Philipp Wahl[b], Myriam Maalaoui[a], Marcus Oel[a], Ina Meyer[a], Berend Denkena[c], Roland Lachmayer[a]

[a]*Institute of Product Development (IPeG), Leibniz University Hannover, An der Universität 1, 30823 Garbsen, Germany*
[b]*Laser Zentrum Hannover e. V., Hollerithallee 8, 30419 Hannover, Germany*
[c]*Institute for Production Engineering and Machine Tools (IFW), Leibniz University Hanover, An der Universität 2, 30823 Garbsen, Germany*

Abstract

Additive manufacturing offers great potential in the aircraft sector due to its high degree of design freedom and new material developments such as Scalmalloy®, a light aluminum alloy with high mechanical properties. Related works show a lack of knowledge about the additive manufacturing of Scalmalloy®, so this paper aims to identify optimal process parameters. A design of experiment is performed, and the hardness, tensile strength, and surface roughness are measured. After that, design parameters are investigated. With the optimized process parameters, a density of 99.87 % is achieved. The hardness is 168.5 HV0.3, and the tensile strength is 541.7 MPa after thermal treatment. Surface roughnesses between 19 and 49 *Ra* are measured depending on the build direction. Minimum manufacturable dimensions are defined for walls, cylinders, and inclination angles. The identified process parameters and the characterization of mechanical properties deliver fundamental knowledge to enable the utilization of Scalmalloy® for aircraft applications.
Keywords: Powder bed fusion of metals using a laser beam (PBF-LB/M); Additive manufacturing; Scalmalloy®; Process parameter development; Aircraft applications

1. Introduction

Additive manufacturing (AM) offers, due to its layer-wise and tool-free production, great design freedoms for highly functional, optimized parts that are difficult or impossible to manufacture with conventional processes (Ehlers et al., 2022; Lachmayer et al., 2024; Wahl et al., 2022). The powder bed fusion of metals using a laser beam (PBF-LB/M) is one of the leading AM processes for metallic parts with high design freedoms (Spierings et al., 2017), which makes it attractive for the aerospace, medical, and automotive sectors (Niedermeyer et al., 2023; Shakil et al., 2023). The rapid solidification due to the focused laser beam and rapid cooling enables the creation of a fine microstructure, resulting in good mechanical properties that are comparable or even superior to those of conventional cast or wrought parts (Bayoumy et al., 2021). For lightweight applications, aluminium alloys with low density and high mechanical properties can be used in PBF-LB/M (Turangi et al., 2020). Scalmalloy® is a zirconium-modified aluminum-scandium-magnesium alloy developed by Airbus Group Innovations specifically for the PBF-LB/M process, which has attracted considerable attention (Shakil et al., 2023). The advantages of Scalmalloy® lie in its high tensile strength of 490-530 MPa with an elongation at break of 8-14 %, high hardness of 165-180 HV0.3, and fatigue and corrosion resistance, combined with a low density of 2.7 g/cm³ compared to other aluminum alloys for the PBF-LB/M process (Cabrera-Correa et al., 2023; Schneller et al., 2021). For this reason, Scalmalloy® is used for many technical applications, particularly in the aerospace and automotive sectors (Shakil et al., 2023). The PBF-LB/M process has several process parameters that directly affect the precipitation behavior, microstructure, part density, and mechanical properties (Spierings et al., 2018). Therefore, understanding the relationships between material properties and process parameters in PBF-LB/M for Scalmalloy® is important (Bayoumy et al., 2021).
This paper aims to develop the essential process parameters for a Scalmalloy® alloy, to characterize the material, and to determine design parameters for producing high-quality parts. The state of the art on process parameters for Scalmalloy® is presented in chapter 2. In chapter 3, the materials and methods considering a design of experiment for process parameter

development, material characterization by hardness and tensile tests, roughness measurements, and design parameter determination are described. The key results are depicted and discussed in chapter 4. The paper concludes with a summary and an outlook on further research in chapter 5.

2. State of the Art

In the PBF-LB/M process, numerous factors influence part quality; up to 130 parameters are presented in the literature (Yadroitsau, 2008). The most important influencing factors are the laser power P, scanning speed v, hatch spacing h_d, and layer thickness d_s (Turangi et al., 2020). The volume energy density E_V is a measure of the energy input per unit volume and is calculated from these variables as follows:

$$E_V = \frac{P}{v \cdot h_d \cdot d_s}$$

(2.1)

The volume energy density E_V is used to determine a parameter range with good melting behavior of the powder (Riener et al., 2022). However, studies show that part properties vary with the same volume energy density and differing process parameters, which is why E_V alone is not appropriate for evaluation (Riener et al., 2022). Better results can be achieved by considering the individual influencing factors P, v, h_d, and d_s. To gather typical process parameters for Scalmalloy®, a keyword search is performed on the Scopus® platform from Elsevier B.V. using the search string:

TITLE-ABS-KEY ("scalmalloy" OR "Al-Sc" OR "AlSc" OR 'AlMgScZr' OR "Al-Mg-Sc-Zr") AND TITLE-ABS-KEY ("selective laser melt*" OR "powder bed fusion").

The literature search yielded 69 English-language, open-access documents. Previous studies give wide ranges of values for P, v, h_d, and d_s, with optimal volume energy densities ranging between 50 and 266.7 J/mm³. Table 1 summarizes the process parameters, volume energy densities, and utilized PBF-LB/M machines of key papers.

Table 1: Process parameters, volume energy densities, and machines in the literature of Scalmalloy®

Laser Power P [W]	Scanning speed v [mm/s]	Hatch spacing h_d [µm]	Laser focus diameter d [µm]	Layer thickness d_s [µm]	Volume energy density E_V [J/mm³]	PBF-LB/M machine	Reference
300-370	800-1600	100	100	30	62,5-154,2	N.D.	(Bayoumy et al., 2021)
340	1600	100	80	30	70,8	N.D.	(Deillon et al., 2022)
360	600	100	100	30	200	EOS M290	(Ekubaru et al., 2022)
250-350	1218-3410	60-120	80	30	20,4-159,6	EOS M290	(Großmann et al., 2020)
350	1400	100	150	50	50	N.D.	(Jeyaprakash et al., 2022)
200	500	50	70	30	266,7	Renishaw AM400	(Kuo et al., 2020)
375	900	100	82	60	69,4	SLM 280HL	(Koutny et al., 2018)
320	1300-2000	N.D.	N.D.	N.D.	60-90	N.D.	(Lasagni et al., 2022)
170	800	100	40	30	70,8	EOS M100	(Mehta et al., 2022)
370	1600	70	100	30	110,1	EOS M290 / N.D.	(Musekamp et al., 2021)
370	1000	100	100	30	123,3	EOS M280	(Nezhadfar et al., 2021)
200	170	150	100	30	260	ConceptLaser M2	(Spierings et al., 2016)
200	350/170	165	100	30	115/238	ConceptLaser M2	(Spierings et al., 2017)
200	<320/<395	165/135	100	30	>125	ConceptLaser M2	(Spierings et al., 2018)
370	1000	100	80	30	123,3	Aconity® Midi	(Schimbäck et al., 2022)
400	808-1270	150	70	30	70-110	Renishaw AM400	(Turangi et al., 2020)

Microstructural investigations on Scalmalloy® reveal a bimodal grain structure consisting of Al_3Sc and Mn(Fe) phases with finer grains along the melt pool boundaries and coarser grains within the melt pool (Bayoumy et al., 2021). The high cooling rates in PBF-LB/M lead to the formation of an oversaturated mixed crystal and the fine dispersion of $Al_3(Sc, Zr)$ phases in Scalmalloy® (Schmidtke et al., 2011). These phases act as nucleation sites and lead to a solidification mechanism, as

dislocations are impeded and grain boundaries are stabilized, which improves the mechanical properties (Schmidtke et al., 2011). The precipitates limit the formation of columnar grains, which are more susceptible to hot cracking during solidification (Schmidtke et al., 2011). Due to the fine-grained microstructure, the anisotropy is reduced compared to other additively manufactured aluminum alloys (Spierings et al., 2016). Spierings et al. confirm the correlation between process parameters and the precipitation of $Al_3(Sc, Zr)$ phases, which influences the density and mechanical properties of Scalmalloy® (Spierings et al., 2017; Spierings et al., 2018). Tensile tests show that the tensile strength varies only slightly (less than 5 %) depending on the build direction of 0, 45, and 90 ° (Schmidtke et al., 2011). As a heat treatment for Scalmalloy®, a temperature of 325 °C for four hours is established (Cabrera-Correa et al., 2023). The thermal treatment leads to the reduction of residual stresses (Cabrera-Correa et al., 2023) and to the improvement of mechanical properties through precipitation hardening (Musekamp et al., 2021). Secondary $Al_3(Sc, Zr)$ phases are precipitated, which stabilize the grain boundaries and cause a fine-grained microstructure (Musekamp et al., 2021). This leads to an increase in tensile strength of 46 % and yield strength of 76 %, while elongation at break decreases by 36 % (Musekamp et al., 2021).

3. Materials and Methods

For the following investigations, Scalmalloy® powder from the manufacturer APWORKS GmbH with a particle size distribution of 20 to 63 µm is used as material. A MIDI+ machine from Aconity3D GmbH is used to process the Scalmalloy® powder in PBF-LB/M (Niedermeyer et al., 2025). Previous studies reveal increased porosity and differences in the microstructure of Scalmalloy® when using a platform heating (Riener et al., 2022), so this is not used in this work. The investigations begin with a design of experiment for relevant process parameters and an experimental analysis of the relative density in section 3.1. A process parameter combination is selected from the analysis, and the hardness and tensile strength are characterized in section 3.2. The surface roughness is measured in different build directions in section 3.3. The method concludes with the determination of dimensional design parameters for the wall thickness, cylinder diameter, and inclination angle in section 3.4.

3.1. Process parameters for high relative density

The process parameters for Scalmalloy® are developed and modeled by creating sensitivity and prediction analysis diagrams. The goal is to maximize relative density by adapting the most important process parameters laser power P, scanning speed v, and hatch spacing h_d. To reduce the scope of testing, the layer thickness d_s is set to 30 µm. A central composite design (CCD) with five factor levels and orthogonal star points is used to identify non-linear effects, and their interactions. The factor level values are defined according to the literature and a parameter set from the powder manufacturer. The laser power P is defined for the upper star point (α) at 395 W, as this is the maximum achievable power of the Aconity MIDI+ machine. The upper factor level of the cube (+) is defined as 370 W from the parameter set. The scanning speed v and hatch spacing h_d are set to 1350 mm/s and 100 µm for the center (0), according to the parameter set by the powder manufacturer. From the literature in Table 1, the scan speed v is selected as 1000 mm/s (Schimbäck et al., 2022) and the hatch spacing h_d as 70 µm (Musekamp et al., 2021) for the lower factor level of the cube (-). All other values are calculated using the previously defined values with a linear relationship. A CCD consisting of a full factorial cube with center and star points is constructed from the factor level values. The center is designed three times to enable a statistical statement about the dispersion with the same process parameters. Table 2 shows the CCD. This provides parameter combinations that cover volume energy densities between 34 and 176 J/mm³, thus reflecting the range of values found in the literature.

Table 2: Central composite design of experiment for the process parameter development of laser power P, scanning speed v, and hatch spacing h_d

Sample	P1	P2	P3	P4	P5	P6	P7	P8	P9	P10	P11	P12	P13	P14	P15-17
Position	5	17	11	6	4	12	1	10	2	8	3	9	14	16	15, 7, 13
P [W]	228.4 (-)	370 (+)	228.4 (-)	370 (+)	228.4 (-)	370 (+)	228.4 (-)	370 (+)	203.4 (-α)	395 (α)	299.2 (0)	299.2 (0)	299.2 (0)	299.2 (0)	299.2 (0)
v [mm/s]	1000 (-)	1000 (-)	1700 (+)	1700 (+)	1000 (-)	1000 (-)	1700 (+)	1700 (+)	1350 (0)	1350 (0)	876.5 (-α)	1823.5 (α)	1350 (0)	1350 (0)	1350 (0)
h_d [µm]	70 (-)	70 (-)	70 (-)	70 (-)	130 (+)	130 (+)	130 (+)	130 (+)	100 (0)	100 (0)	100 (0)	100 (0)	59.4 (-α)	140.6 (α)	100 (0)
E_V [J/mm³]	108.7	176.1	63.98	103.6	58.56	94.87	34.45	55.81	50.22	97.53	113.7	54.69	124.3	52.54	73.88
Note	"Cube" full factorial								"Stars" any factor separated						"Center" 3 times

The samples from the CCD are designed as test cubes with an edge length of 10 mm and manufactured on the machine in one production process. Positioning on the build platform is randomized (see Table 2), and the cubes are rotated 45 ° to the coating direction to generate low contact forces. A strip pattern is selected as the scanning strategy, which is rotated by 67 ° after each layer. To examine the layer bonding of a contour parameter set, two contour lines with a laser power of 370 W and a scanning speed of 1000 mm/s, according to the powder manufacturer's parameter set, are added. The cubes are manufactured on support structures and then embedded, sanded, and polished. The relative density is determined using light microscopic images taken with a KEYENCE DEUTSCHLAND GMBH VHX-900F digital microscope at a magnification of 100, followed by evaluation using a python script that performs a black-and-white comparison and calculates the pore area to the metal area. The statistical evaluation is performed using the JMP® software developed by SAS INSTITUTE GMBH. An effect screening is performed to determine the main effects and interactions of the factors on the relative density. A regression analysis based on the least squares method is calculated, and the coefficient of determination R^2 is determined. Subsequently, an optimal parameter combination using the prediction analysis diagram and the best sample from the CCD are selected and manufactured three times for validation.

3.2. Hardness and tensile strength

The mechanical properties from the selected parameter combination are characterized in the as-built and heat-treated states. Precipitation hardening in a furnace at 325 °C for four hours is performed as heat treatment. A Vickers hardness test by DIN EN ISO 6507-1 (DIN-Normenausschuss Materialprüfung, 2024) is performed on a VHT-500C digital macro Vickers hardness tester from 3-RATH, and the hardness value HV0.3 is determined. The hardness test is performed on the side surface of the samples in Figure 1 in as-built and heat-treated conditions for three samples each. Five indentations in a star pattern are made for each sample, and the mean value is calculated. A tensile test is performed according to DIN 50125 (DIN-Normenausschuss Materialprüfung, 2022) on a Z010 universal testing machine from ZWICK ROELL and evaluated using testXpert III software. Three flat samples in as-built and heat-treated conditions are produced from an additively manufactured blank with subsequent machining in the form specified in DIN 50125-E2x6x20. The tensile strength is calculated, and the elongation of the sample is measured by the software based on the distance traveled by the crosshead.

3.3. Surface roughness depending on build direction

The surface roughness is measured on 12 samples according to Figure 1 using the mean roughness value *Ra*. Since roughness depends on the part orientation (Lachmayer et al., 2024), it is determined on the top, upskin, downskin, and side surface. The downskin surface is designed at an inclination angle of 45 ° without support structures. The roughness is measured on three samples in the as-printed and heat-treated state, as well as with and without two contour lines in accordance with section 3.1. Roughness is measured by DIN EN ISO 4288 (DIN Normenausschuß Technische Grundlagen, 1998) using a VK-X1000 confocal 3D laser scanning microscope from Keyence Deutschland GmbH. The evaluation is performed using the MultiFileAnalyzer software. The surface roughness of Scalmalloy® is estimated to be between 5 and 25 µm based on the literature (Musekamp et al., 2021), which is why five individual measuring sections of 8 mm are selected for all surfaces. A profile filter λ_c of 8 mm and a low-pass filter λ_s of 25 µm are applied to filter out waviness and noise by VDI/VDE 2602 (VDI/VDE-Gesellschaft Mess- und Automatisierungstechnik, 2018).
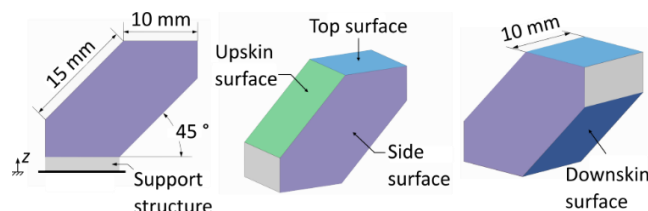

Figure 1: Design of the surface roughness samples and the analysed top, upskin, downskin, and side surface depending on the build direction *z*

3.4. Dimensional design parameters

The minimum manufacturable dimensions for the design of parts are investigated for the selected parameter combination. The sample design and dimensions are presented in Figure 2; these are oriented on VDI 3405-3.2 (VDI-Gesellschaft Produktion und Logistik, 2019), whereby the minimum manufacturable wall thickness d_W, cylinder diameter D_Z, and

inclination angle β are addressed. The inclined beams are manufactured without support structures. The wall thicknesses and cylinder diameters are first assessed visually and then measured 10 times for each dimension using a VHX-990F digital microscope from KEYENCE DEUTSCHLAND GMBH, with a subsequent average determination. The ratio between the real and ideal dimensions according to CAD is calculated. The inclination angle is visually assessed by the manufactured beams.
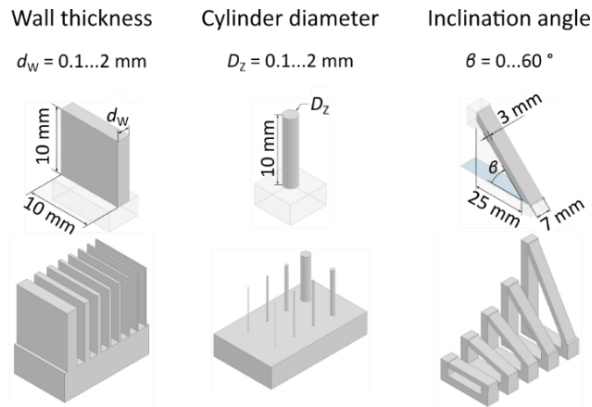

Figure 2: Design of the design parameter samples: minimum wall thickness d_W, minimum cylinder diameter D_Z, and minimum inclination angle β

4. Results and Discussion

4.1. Process parameters and relative density

The manufactured samples show clear differences in overall porosity. The relative density shows that 9 of 17 samples achieve a relative density above 99 %. Figure 3 on the left shows light microscope images of samples P7 and P2, which have the lowest and highest relative densities at 91.52 % and 99.87 %. Sample P7 has more and larger pores than P2. The contour parameters achieve a good connection to the internal volume, which is why this set of contour parameters will continue to be used. Figure 3 on the right shows the relative density plotted against the volume energy density. The volume energy density exhibits highly nonlinear behavior, and the relative density varies with changing process parameters at the same volume energy density. The lowest density corresponds to the lowest volume energy density, while the highest density occurs at the highest volume energy density. However, this relationship is not apparent for the other parameter combinations. The standard deviation from the values for the center point with P15 to P17 is 0.15 %.
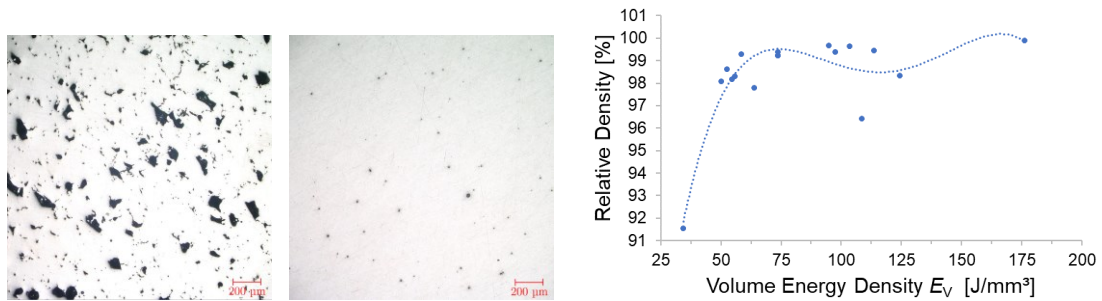
Figure 3: Light microscope images of the samples P7 (left), P2 (center), and relative density over volume energy density (right)

The regression analysis in JMP® yields a model with a coefficient of determination of $R^2 = 0.93$, while the sample P7 lies outside the 95 % confidence interval in the studentized residuals and is excluded. The effects and interactions of the process parameters are calculated using the p-value and shown in Table 4. The laser power P has the lowest p-value of 0.00134 and thus the highest significance for relative density. The interaction between laser power and hatch spacing $P \cdot h_d$ shows significance with a p-value of 0.00755. The interaction between scanning speed and hatch spacing $v \cdot h_d$ can be identified as indifferent. All other effects are considered insignificant.

Table 3: Significance of the effects and interaction of effects with the *p*-Value

Effect and interaction of effects	*p*-Value	Significance niveau	Denotation
Laser power P	0,00134	**	Significant
Laser power · hatch spacing $P \cdot h_d$	0,00755	**	Significant
Scanning speed · hatch spacing $v \cdot h_d$	0,03538	*	Indifferent
Hatch spacing · hatch spacing h_d^2	0,08745	-	Not significant
Scanning speed v	0,10903	-	Not significant
Hatch spacing h_d	0,12110	-	Not significant
Laser power · scanning speed $P \cdot v$	0,14758	-	Not significant
Laser power · laser power P^2	0,33048	-	Not significant
Scanning speed · scanning speed v^2	0,46762	-	Not significant

Prediction analysis diagrams to display the predicted relative density over the main effects are created and shown on the left in Figure 4. The relative density increases with higher laser power, lower scanning speed, and smaller hatch spacing. A calculated optimum for the relative density of 100.8 % is also shown in red. A contour analysis diagram illustrates the interaction between two factors and is shown in Figure 4 on the right for the laser power and hatch spacing. With increasing hatch spacing, an increase in relative density can be seen at low to medium laser powers. At high laser powers, small hatch spacings lead to better relative densities. The current best value of 99.87 % (sample P2) is visualized in blue, while theoretically higher relative densities can be achieved in the white area.
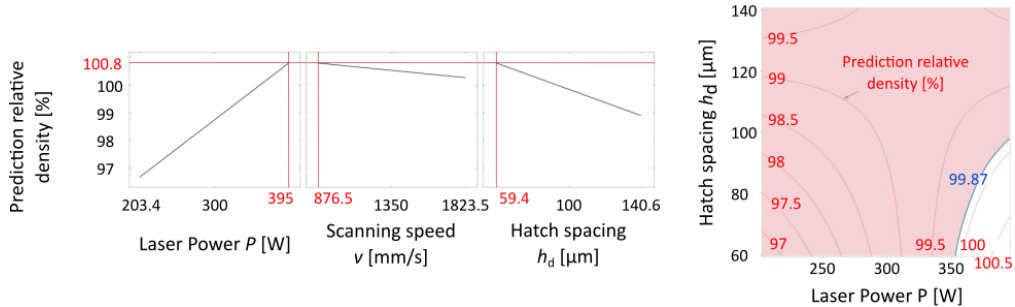
Figure 4: Prediction analysis diagrams of the effects of laser power P, scanning speed v, and hatch spacing h_d (left) and contour analysis diagram of the effects of laser power P and hatch spacing h_d (right)

An optimum parameter combination MAX is selected from the regression model with maximum laser power, minimum scanning speed, and minimum hatch spacing, and compared with the parameter combination P2. The results are shown in Table 5. The mean value from three samples per parameter combination results in a better relative density for sample P2 at 99.85 %. The best individual result is also achieved by a sample from P2 with a relative density of 99.93 %. The results do not indicate an improvement with the optimized parameter combination MAX. Since the best relative density is achieved with sample P2, these process parameters are specified for all further tests.

Table 4: Relative density of the parameter combinations P2 and MAX

Sample	P [W]	v [mm/s]	h_d [µm]	E_V [J/mm³]	Relative density [%]
P2	370	1000	70	176,19	99,85 (+0,09/ - 0,07)
MAX	395	876,5	59,4	252,89	99,84 (+0,04/-0,06)

Light microscope images reveal high porosity for sample P7 with the lowest volume energy density. This may indicate a lack of fusion, in which the powder is not sufficiently melted, resulting in gaps with pores. The sample P2 shows over all tests the best relative density, which can indicate a local optimum. The relative density shows a highly nonlinear behavior over the volume energy density, which illustrates that many influencing factors occur. The standard deviation of 0.15 % supports this statement, as other process variables in the PBF-LB/M process, e.g. scanning strategy or gas flow, are relevant. A measurement error in the evaluation procedure is also possible. The significance analysis shows that the laser power has the greatest influence on the relative density. The laser power determines the amount of energy that acts on the powder

and thus directly influences the melting behavior. The scanning speed has the next largest effect on the relative density, although not significantly. This defines the duration of the interaction between the powder and the laser and thus influences the melt pool dynamics. The hatch spacing has the least effect on the relative density. This describes the overlap of two adjacent scan vectors and thus the connection of the melt pool with the surrounding material. The prediction analysis diagrams show that optimum results can be expected at the limits of the parameter range, with maximum laser power, minimum scanning speed, and minimum hatch spacing. With an enlarged test range with laser powers above 400 W, scan speeds below 875 mm/s, and hatch spacing below 59 μm, better part densities can be achieved and more comprehensive effects can be measured, but the machine specifications are here the limiting factor. The samples with the optimal parameter combination show deviations from the predictions. The values in the model reach relative densities above 100 %, what is not possible, while the actual samples show densities of 99.85 %, close to P2. This can be due to model inaccuracies and disturbance variables in the process.

4.2. Hardness and tensile strength

The average hardness of samples with the parameters of P2 for as-built and heat-treated is displayed in Figure 5 left. The hardness for as-built samples lies between 110.6 and 113.4 HV0.3 with a mean value of 112.3 ± 1.43 HV0.3. The heat-treated samples reach hardnesses between 165.2 and 170.3 HV0.3 with a mean value of 168.5 ± 2.85 HV0.3. This corresponds to an increase of 50 % due to heat treatment. The stress-strain curves for as-built and heat-treated samples are shown in Figure 5 right. The as-built samples show larger deviation and tensile strengths between 356 and 379 MPa with a mean value of 360.3 ± 16.9 MPa. The heat-treated samples show a more uniform curve across the three samples and results in tensile strengths between 536 and 547 MPa with a mean value of 541.7 ± 5.5 MPa. This reveals an increase of the tensile strength of 50 % compared to the as-built samples. The elongation at break of the heat-treated samples decreases by approx. 50 %.
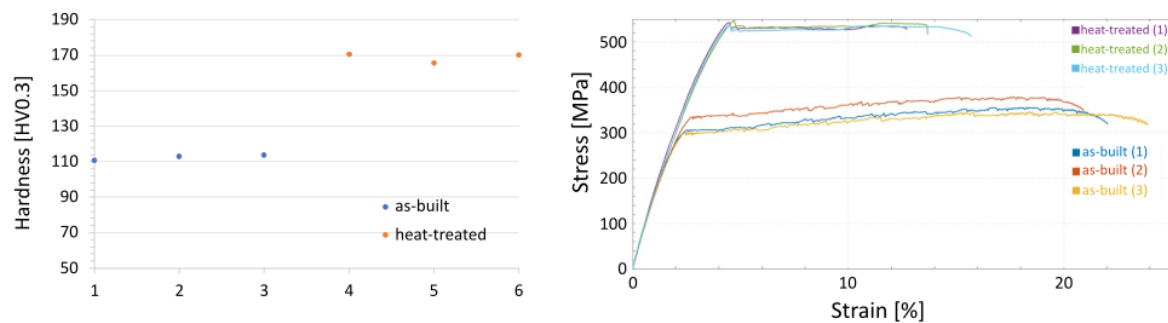

Figure 5: Average hardness for the as-built and heat-treated samples (left) and stress-strain diagram for the as-built and heat-treated samples (right)

The hardness for the heat-treated samples shows values in the range of 165-170 HV 0.3, as in the literature. The tensile strength of the heat-treated samples exceeds the values of 490-530 MPa specified in the literature. The increased strength and hardness can be explained by the precipitation of secondary $Al_3(Sc, Zr)$ phases, which are formed in the temperature range of 325 °C and thus produce a fine microstructure with greater dislocation resistance. The reduction of residual stresses and the homogenization of the microstructure during heat treatment also lead to more uniform strength and lower anisotropy. The elongation at break decreases by the same amount as a result of heat treatment.

4.3. Surface roughness depending on build direction

The average surface roughness *Ra* of the 12 samples for the top (Top), side (S), downskin (D), and upskin (U) surfaces is shown in Figure 6. The table shows the average values of each sample group for the respective surfaces. The top surface shows the lowest *Ra*, averaging between 19.19 and 23.37 μm, followed by the side surface. The downskin surface shows the highest *Ra*, averaging between 40.49 and 48.48 μm. A sample with contour achieves the lowest roughness for the side, downskin, and upskin surfaces, with roughness reduction by approx. 10 % for the downskin and upskin surfaces. Heat treatment increases the roughness of the downskin surface without a contour by 10 %, but no significant influence can be detected overall. The side surfaces show the least impact with contour and heat treatment, and a nearly constant roughness. The standard deviations within the sample groups range between 2 and 75 %. The highest standard deviation shows samples with contour and heat treatment for the top surface, while the side surfaces are comparatively low.
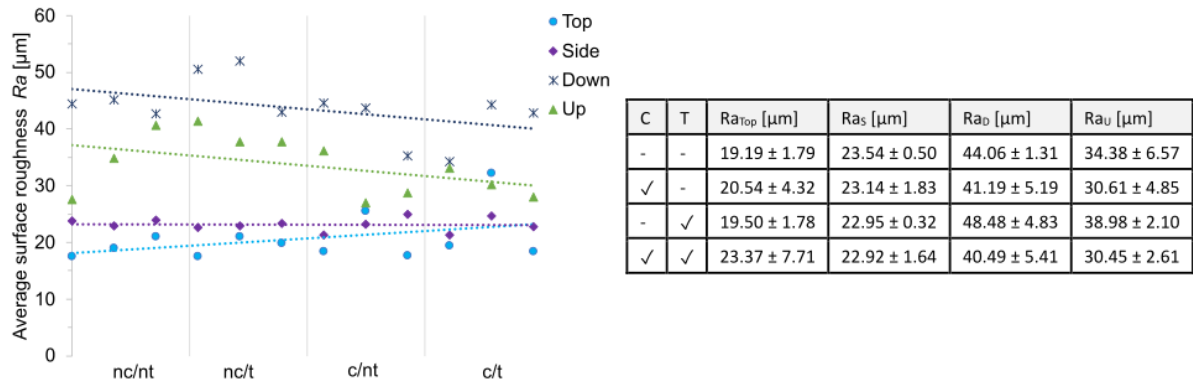
Figure 6: Average surface roughness *Ra* for samples without contour (nc), with contour (c), without thermal treatment (nt), and with thermal treatment (t) for the top (Top), side (S), downskin (D) and upskin (U) surfaces

The surface roughness values can be explained by adhering and incompletely melted powder particles on the surface whose particle diameters range between 15 and 70 μm. These act as additional height structures and increase the roughness. The heat input from the laser beam can cause adjacent powder particles to adhere to the surface or be partially melted. The downskin surface shows the highest roughness, as the laser beam partially penetrates the layer and melts loose powder below, causing it to adhere. The poorer heat dissipation due to the powder bed also leads to more powder adhesion and increased surface roughness. Contour parameters can improve surface roughness via a targeted exposure and heat input on the surface to reduce powder adhering. However, the contour is not applied to the top surface. On upskin and downskin surfaces, the staircase effect appears due to the layer-wise manufacturing, causing higher surface roughness. The standard deviation is low on the side surfaces, as there is less random powder adhesion than on the other surfaces.

4.4. Dimensional design parameters

All samples except the beams with an inclination angle of 15 and 30 ° can be successfully produced. The ratios from real to ideal wall thickness are shown in Figure 7 on the left. At the nominal dimension of 0.1 mm, the real wall thickness is 46 % larger. With increasing nominal dimension, the deviation decreases, first between 101 and 105 % in the range of 0.2-0.5 mm, then levels off at 100 %. A deviation under 5 % first occurs at a wall thickness of 0.2 mm. The ratios of real to ideal cylinder diameter are shown in Figure 7 in the center. Since the cylinder diameter of 0.1 mm broke off during unpacking, the results start at 0.2 mm. At 0.2 mm, the real diameter is increased by 16.5 %. After that, the same course appears as for the wall thickness. A deviation under 5 % first occurs at a cylinder diameter of 0.3 mm. The samples for the minimum inclination angle are shown in Figure 7 on the right. The beam with an inclination angle of 0 ° can be completed and shows a porous and uneven structure on the bottom side. Some powder deposits and partially melted material are visible. The beams with an inclination angle of 15 and 30 ° show unevenness, which leads to their abortion. The bottom side is curved and porous, and the top side is warped up. At 30 °, an even structure is visible in the first layers until the defects occur. The beam with an inclination angle of 45 ° is successfully manufactured, but shows individual unevenness on the bottom side at higher layers. The beam with an inclination angle of 60 ° shows no defects over the entire length.
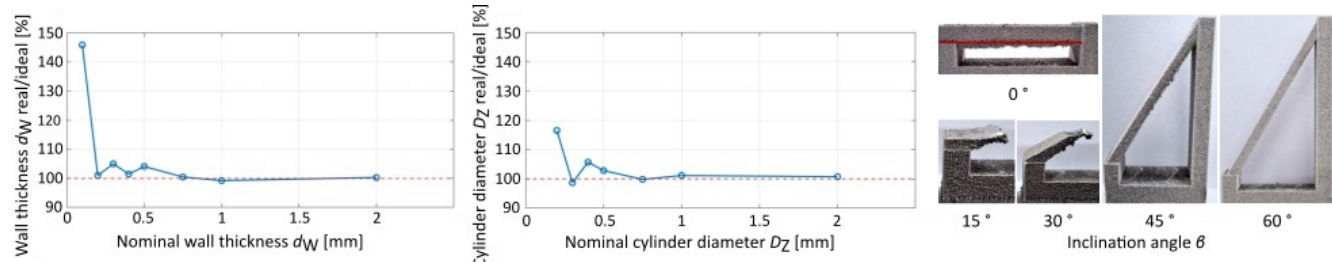

Figure 7: Ratio of real to ideal wall thickness over the nominal wall thickness (left), ratio of real to ideal cylinder diameter over the nominal cylinder diameter (center), and images of the beams with inclination angles (right)

The large deviations at low dimensions are due to the larger heat-affected zone. The focus diameter on the machine is 0.1 mm, which means that the laser beam heats the surrounding powder and melts it, resulting in a larger geometry. Starting at dimensions of 0.2 mm, scan vectors can be overlapped, and the deviations can be reduced until the real part is near the ideal geometry. The beam with an inclination angle of 0 ° is successfully produced because it is sufficiently supported on both side walls so that it does not sink completely into the powder bed. Nevertheless, large unevennesses occur on the bottom side because the powder underneath is partially melted, and due to a lack of support sinks into the powder bed. With increasing contact area with the side walls, the beam stabilizes itself further over the height until a solid structure occurs. In the case of the beams with 15 and 30 °, there is no opposite side wall for stabilization, so a porous, curved structure forms on the bottom side, and warping occurs on the top side. The curved structure results from losing a part of the molten material due to less connection to the beam and falling into the powder bed. Overheating and warping occur on the tip of the beam due to the high heat input on low-bonded material with low heat conduction. These effects reduce when the inclination angle increases until no defects appear. At an inclination angle of 45 °, there is sufficient support material from the beam below, resulting in less distortion. The beam with an inclination angle of 60 ° achieves more support, resulting in no defects. Due to the close approximation between real and ideal geometry under 5 %, a wall thickness of 0.2 mm and a cylinder diameter of 0.3 mm are considered to be the minimum manufacturable dimensions. Based on the defects observed on the beams, a minimum manufacturable inclination angle without support structures is defined as 45 °. The determined minimum manufacturable design parameters are summarized in Table 7.

Table 5: Minimum manufacturable design parameters wall thickness d_W, cylinder diameter D_Z, and inclination angle β

Design parameter	Wall thickness d_W	Cylinder diameter D_Z	Inclination angle β
Minimum manufacturable dimension	0.2 mm	0.3 mm	45 °

5. Conclusion and Outlook

In this paper, process parameters for Scalmalloy® in PBF-LB/M are developed using a design of experiment and then characterized for mechanical properties, surface roughness, and design parameters. A central composite design is performed to develop a prediction model for relative density as a function of laser power P, scanning speed v, and hatch spacing h_d. With this, an optimal parameter combination is selected, for which the hardness and tensile strength in as-built and heat-treated states are determined. The surface roughness is measured on the top, upskin, downskin, and side surfaces for as-built, heat-treated samples, and for samples with and without contour lines. Design parameters for minimum manufacturable wall thickness, cylinder diameter, and inclination angle are determined by samples. The prediction model can be used to determine relative densities for Scalmalloy® under various process parameters. A process parameter combination with a high relative density of 99.87 % is developed. Heat treatment can increase the hardness and tensile strength by 50 % to 168.5 HV0.3 and 541.7 MPa. The lowest surface roughness occurs on the top surface, with 19.19 to 23.37 µm Ra, while the downskin surface achieves the highest roughness of 40.49 to 48.48 µm. Contour parameters can reduce roughness by approx. 10 %, while heat treatment shows no effect. The minimum manufacturable design parameters for Scalmalloy® are wall thicknesses of 0.2 mm, cylinder diameters of 0.3 mm, and inclination angles of 45 °.

In further work, the developed prediction model can be supplemented by additional influencing factors, such as scanning strategy or layer thickness, and an extended parameter range with higher laser power, lower scanning speed, and smaller hatch spacing. With this, more reliable predictions and higher relative densities can be realized. A contour parameter study can be done to reduce the surface roughness and to minimize post-processing steps. In addition, further design parameters will need to be developed in the future to provide all relevant manufacturing restrictions for the design.

References

Bayoumy, D., Schliephake, D., Dietrich, S., Wu, X. H., Zhu, Y. M., & Huang, A. J. (2021). Intensive processing optimization for achieving strong and ductile Al-Mn-Mg-Sc-Zr alloy produced by selective laser melting. Materials & Design, 198, 109317. https://doi.org/10.1016/j.matdes.2020.109317

Cabrera-Correa, L., González-Rovira, L., Dios López-Castro, J. de, Castillo-Rodríguez, M., & Botana, F. J. (2023). Effect of the heat treatment on the mechanical properties and microstructure of Scalmalloy® manufactured by Selective Laser Melting (SLM) under certified conditions. Materials Characterization, 196, 112549. https://doi.org/10.1016/j.matchar.2022.112549

Deillon, L., Jensch, F., Palm, F [F.], & Bambach, M. (2022). A new high strength Al–Mg–Sc alloy for laser powder bed fusion with calcium addition to effectively prevent magnesium evaporation. Journal of Materials Processing Technology, 300, 117416. https://doi.org/10.1016/j.jmatprotec.2021.117416

DIN Normenausschuß Technische Grundlagen (April 1998). Geometrische Produktspezifikationen (GPS) Oberflächenbeschaffenheit: Tastschnittverfahren: Regeln und Verfahren für die Beurteilung der Oberflächenbeschaffenheit (DIN EN ISO 4288).

DIN-Normenausschuss Materialprüfung (August 2022). Prüfung metallischer Werkstoffe - Zugproben (DIN 50125).

DIN-Normenausschuss Materialprüfung (Januar 2024). Metallische Werkstoffe –Härteprüfung nach Vickers: Teil 1: Prüfverfahren (ISO 6507-1:2023) (DIN EN ISO 6507-1).

Ehlers, T., Meyer, I., Oel, M., Bode, B., Gembarski, P. C., & Lachmayer, R. (2022). Effect-Engineering by Additive Manufacturing. Innovative Product Development by Additive Manufacturing 2021, 1–19. https://doi.org/10.1007/978-3-031-05918-6_1

Ekubaru, Y., Gokcekaya, O., Ishimoto, T., Sato, K., Manabe, K., Wang, P., & Nakano, T. (2022). Excellent strength–ductility balance of Sc-Zr-modified Al–Mg alloy by tuning bimodal microstructure via hatch spacing in laser powder bed fusion. Materials & Design, 221, 110976. https://doi.org/10.1016/j.matdes.2022.110976

Großmann, A., Mölleney, J., Frölich, T., Merschroth, H., Felger, J., Weigold, M., Sielaff, A., & Mittelstedt, C. (2020). Dimensionless process development for lattice structure design in laser powder bed fusion. Materials & Design, 194, 108952. https://doi.org/10.1016/j.matdes.2020.108952

Jeyaprakash, N., Yang, C.-H., & Kumar, M. S. (2022). Influence of coherent intermetallic nano-precipitates on the nano-level mechanical and tribological properties of the Laser-Powder bed fused Scalmalloy. Materials Characterization, 193, 112269. https://doi.org/10.1016/j.matchar.2022.112269

Koutny, D., Skulina, D., Pantělejev, L., Paloušek, D., Lenczowski, B., Palm, F [Frank], & Nick, A. (2018). Processing of Al-Sc aluminum alloy using SLM technology. Procedia CIRP, 74, 44–48. https://doi.org/10.1016/j.procir.2018.08.027

Kuo, C. N., Chua, C. K., Peng, P. C., Chen, Y. W., Sing, S. L., Huang, S., & Su, Y. L. (2020). Microstructure evolution and mechanical property response via 3D printing parameter development of Al–Sc alloy. Virtual and Physical Prototyping, 15(1), 120–129. https://doi.org/10.1080/17452759.2019.1698967

Lachmayer, R., Ehlers, T., & Lippert, R. B. (2024). Design for Additive Manufacturing. Springer Berlin Heidelberg. https://doi.org/10.1007/978-3-662-68463-4

Lasagni, F., Galleguillos, C., Herrera, M., Santaolaya, J., Hervás, D., González, S., & Periñán, A. (2022). On the processability and mechanical behavior of Al–Mg–Sc alloy for PBF-LB. Progress in Additive Manufacturing, 7(1), 29–39. https://doi.org/10.1007/s40964-021-00216-z

Mehta, B., Svanberg, A., & Nyborg, L. (2022). Laser Powder Bed Fusion of an Al-Mg-Sc-Zr Alloy: Manufacturing, Peak Hardening Response and Thermal Stability at Peak Hardness. Metals, 12(1), 57. https://doi.org/10.3390/met12010057

Musekamp, J., Reiber, T., Hoche, H. C., Oechsner, M., Weigold, M., & Abele, E. (2021). Influence of LPBF-Surface Characteristics on Fatigue Properties of Scalmalloy®. Metals, 11(12), 1961. https://doi.org/10.3390/met11121961

Nezhadfar, P. D., Thompson, S., Saharan, A., Phan, N., & Shamsaei, N. (2021). Structural integrity of additively manufactured aluminum alloys: Effects of build orientation on microstructure, porosity, and fatigue behavior. Additive Manufacturing, 47, 102292. https://doi.org/10.1016/j.addma.2021.102292

Niedermeyer, J., Ehlers, T., & Lachmayer, R. (2023). Potential of additively manufactured particle damped compressor blades: A literature review. Procedia CIRP, 119, 570–575. https://doi.org/10.1016/j.procir.2023.02.151

Niedermeyer, J., Oel, M., Meyer, I., Stauß, T., Mesecke, L., Maalaoui, M., Gerhards, P., Bitter-Davidts, J., Eibl, F., Ehlers, T., & Lachmayer, R. (2025). Konzept einer additiven Großfertigungsanlage zur skalenunabhängigen additiven Fertigung und Reparatur. In R. Lachmayer, M. Oel, & S. Kaierle (Eds.), Innovative Produktentwicklung durch additive Fertigung (pp. 1–16). Springer Berlin Heidelberg. https://doi.org/10.1007/978-3-662-69327-8_1

Riener, K., Pfalz, T., Funcke, F., & Leichtfried, G [Gerhard] (2022). Processability of high-strength aluminum 6182 series alloy via laser powder bed fusion (LPBF). The International Journal of Advanced Manufacturing Technology, 119(7-8), 4963–4977. https://doi.org/10.1007/s00170-022-08673-8

Schimbäck, D., Mair, P., Kaserer, L., Perfler, L., Palm, F [F.], Leichtfried, G [G.], & Pogatscher, S. (2022). An improved process scan strategy to obtain high-performance fatigue properties for Scalmalloy®. Materials & Design, 224, 111410. https://doi.org/10.1016/j.matdes.2022.111410

Schmidtke, K., Palm, F [F.], Hawkins, A., & Emmelmann, C. (2011). Process and Mechanical Properties: Applicability of a Scandium modified Al-alloy for Laser Additive Manufacturing. Physics Procedia, 12, 369–374. https://doi.org/10.1016/j.phpro.2011.03.047

Schneller, W., Leitner, M., Leuders, S., Sprauel, J. M., Grün, F., Pfeifer, T., & Jantschner, O. (2021). Fatigue strength estimation methodology of additively manufactured metallic bulk material. Additive Manufacturing, 39, 101688. https://doi.org/10.1016/j.addma.2020.101688

Shakil, S. I., González-Rovira, L., Cabrera-Correa, L., Dios López-Castro, J. de, Castillo-Rodríguez, M., Botana, F. J., & Haghshenas, M. (2023). Insights into laser powder bed fused Scalmalloy®: investigating the correlation between micromechanical and macroscale properties. Journal of Materials Research and Technology, 25, 4409–4424. https://doi.org/10.1016/j.jmrt.2023.06.228

Spierings, A. B., Dawson, K., Heeling, T., Uggowitzer, P. J [P. J.], Schäublin, R., Palm, F [F.], & Wegener, K. (2017). Microstructural features of Sc- and Zr-modified Al-Mg alloys processed by selective laser melting. Materials & Design, 115, 52–63. https://doi.org/10.1016/j.matdes.2016.11.040

Spierings, A. B., Dawson, K., Uggowitzer, P. J [P. J.], & Wegener, K. (2018). Influence of SLM scan-speed on microstructure, precipitation of Al3Sc particles and mechanical properties in Sc- and Zr-modified Al-Mg alloys. Materials & Design, 140, 134–143. https://doi.org/10.1016/j.matdes.2017.11.053

Spierings, A. B., Dawson, K., Voegtlin, M., Palm, F [Frank], & Uggowitzer, P. J [Peter J.] (2016). Microstructure and mechanical properties of as-processed scandium-modified aluminium using selective laser melting. CIRP Annals, 65(1), 213–216. https://doi.org/10.1016/j.cirp.2016.04.057

Turangi, C., Haslich, F., & Tim Pasang (2020). An Investigation of the Influence of Changing Energy Volume Densities to Produce a Complete Process Parameter Window for Selective Laser Melting of Scalmalloy. In Nusantara Science and Technology Proceedings (pp. 21–33). Galaxy Science. https://doi.org/10.11594/nstp.2020.0503

VDI/VDE-Gesellschaft Mess- und Automatisierungstechnik (April 2018). Oberflächenprüfung Rauheitsmessung mit Tastschnittgeräten: Aufbau, Messbedingungen, Durchführung (VDI/VDE 2602 Part 2).

VDI-Gesellschaft Produktion und Logistik (Juli 2019). Additive Fertigungsverfahren Gestaltungsempfehlungen: Prüfkörper und Prüfmerkmale für limitierende Geometrieelemente (VDI 3405 Sheet 3.2).

Wahl, J. P., Niedermeyer, J., Bernhard, R., Hermsdorf, J., & Kaierle, S. (2022). Design of additively manufacturable injection molds with conformal cooling. Procedia CIRP, 111, 97–100. https://doi.org/10.1016/j.procir.2022.08.146

Yadroitsau, I. (2008). Direct manufacturing of 3D objects by selective laser melting of metal powders [Dissertation, Université Jean Monnet, Saint-Etienne]. RIS. https://theses.fr/2008stet4006